Astron. Astrophys. 267, 199–212 (1993)

ASTRONOMY
AND
ASTROPHYSICS

Spectroscopy and shock modelling of the unusual bipolar outflow NGC 6905

L. Cuesta, J. P. Phillips, and A. Mampaso

Instituto de Astrofisica de Canarias, E-38200 La Laguna, Tenerife, Spain

Received December 27, 1991; accepted May 10, 1992

Abstract. We present high and low resolution multi-slit spectroscopy, together with *V*, [O III] and Hα narrow band imaging of the unusual bipolar outflow source NGC 6905. As a consequence, we are able to investigate the excitation structure of the source, the properties of the central star, and the projected kinematic structure of the outflow shell. Comparison of these results with simplified models of the source suggest that the outflow kinematics of the central shell and lobal extensions are likely to differ appreciably; and this, together with a variety of other evidence, suggests a model in which collimated winds are shock interacting with an enveloping halo. Such a mechanism would not only account for the morphology of the lobes, and the broad variations in surface brightness and excitation, but also matches the observed shell kinematics, and goes some way to explaining the location and characteristics of the associated ansae.

Key words: planetary nebulae – optical spectroscopy – narrow band imaging – shock models

1. Introduction

NGC 6905 is an unusual high excitation nebula characterised by an intense and broadly spheroidal interior shell, dimensions of 47×34 arcsec^2, surmounted by roughly conical extensions extending over a range $\sim 100''$, and strong ansae-type formations at the limits of the major axis. The principal axis has a position angle (PA) of 163° (Perek & Kohoutek 1967), whilst the core ellipsoid appears to be inclined at $\sim 60°$ to the line-of-sight (Sabbadin & Hamzaoglu 1982).

In the following, we present a broad range of spectroscopic observations of NGC 6905 in the wavelength range $\lambda\lambda$4400–6700 Å with the aim of evaluating the physical state, structure and kinematics of the nebular halo, as well as using both these and direct imaging results to investigate kinematic and morphological models of the source.

2. Observations

2.1. Optical spectroscopy

Optical spectroscopy of NGC 6905 was acquired during 1st and 2nd September 1987, using an Intermediate Dispersion Spectrograph (IDS), a 500 mm camera, and a CCD detection element, mounted at the Cassegrain focus of the 2.5 m (f/15) Isaac Newton Telescope (INT) at the Observatorio del Roque de los Muchachos (La Palma, Spain). Two gratings were employed: one (high resolution, H1800V grating) yielding a dispersion of 10.5 Å mm^{-1} over a spectral range of 120 Å centred at Hα, giving a spectral resolution of 0.22 Å pixel^{-1}; the other (low resolution, R150V grating) having a dispersion of 132.2 Å mm^{-1} covering the spectral range from 4400 Å to 6700 Å, and yielding a spectral resolution of 2.9 Å pixel^{-1}. In both of these cases, the slit length was 180″, and the effective spatial resolution 0″.33 pixel^{-1}.

In the high resolution mode, the 1″ slit was positioned at six PA across the central star; three close to the axis of the nebula (PA 340°, 347° and 333°) and three separated by steps of 45° (PA 70°, 115° and 205°; see Fig. 1). In the low spectral resolution mode the slit was placed close to the major axis of the nebula, along a PA of 340°.

Seeing was of the order of 1″.3 during the whole observing period, whilst exposure times were typically 1000 s.

Finally, the wavelength calibration was undertaking using a standard PANDORA package, and provided a calibration better than 0.05 Å and 1 Å for the high and low spectral resolution frames respectively. The extinction correction and flux calibration were made using the standard star Feige 15 (Stone 1977), by employing a standard FIGARO data reduction package, and employing an extinction curve appropriate to the Observatorio del Roque de los Muchachos.

Figure 1 shows the slit positions superimposed on our [O III] image of the source, whilst Fig. 2 shows our high resolution spectrum taken along the major axis of nebula (PA 340°).

2.2. Direct imaging

The nebula was observed during 10th June 1990, using the 2.56 m Nordic Optical Telescope (NOT) at the Observatorio del Roque de los Muchachos (La Palma, Spain). As a result, we were able to acquire exposures in Hα, [O III] and *V*, using the Stockholm CCD camera mounted at the Cassegrain f/11.0 focus. In all cases, the effective spatial resolution was approximately 0.2×0.2 arcsec^2, and local seeing was 1″.4.

The width of the narrow band filters was 20 Å, and the central wavelengths 6563 Å and 5010 Å for Hα and [O III] respectively. The Hα filter also includes emission from the [N II] doublet (6548–6584 Å), corresponding to about 20% transmission for [N II] 6548 Å, and 10% for [N II] 6584 Å. As a result, we estimate that typical contamination of Hα by the [N II] lines is small, and of

Send offprint requests to: L. Cuesta

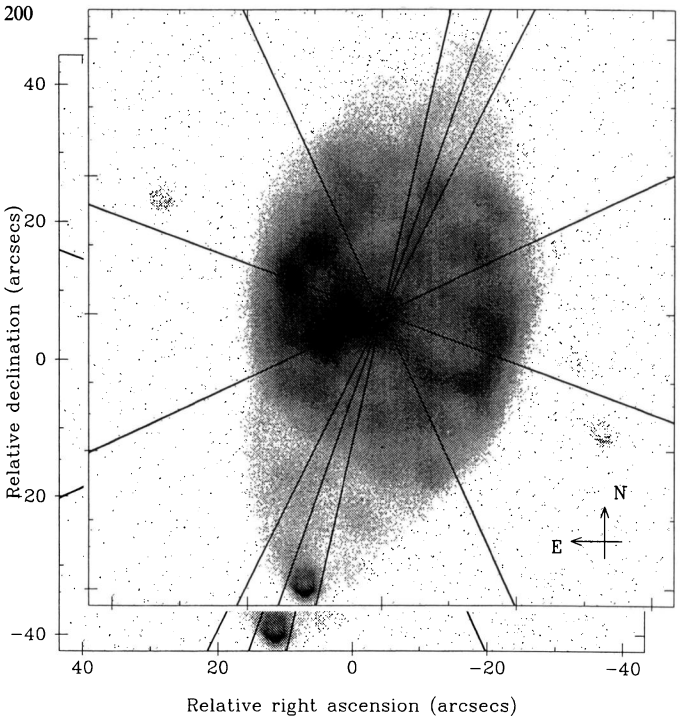

Fig. 1. Slit positions for high and low resolution optical spectroscopy, superimposed upon our [O III] image of NGC 6905

order $\sim 4\%$ (although this must vary of course with position inside the nebula, given the differing [N II]/Hα emission distributions). For the case of the V filter, in comparison, the overall bandwidth was 50 Å centred on 5110 Å. All of these filters had a peak transmission of about 60%.

Finally, the reduction, extinction correction and flux calibration were in all cases undertaken as described in Sect. 2.1 above.

Figure 3 shows the three images observed here, together with a fourth panel illustrating the ratio between Hα and [O III] (see below).

3. Results

3.1. *The O VI sequence nucleus*

The nucleus of NGC 6905 possesses one of the most broadened O VI emission lines yet observed among planetary nebulae (PN) (Johnson 1976; Johnson 1981; Feibelman 1982). Figure 4 shows the low resolution spectrum for the central star in the range $\lambda\lambda$ 4350–5950 Å, revealing the presence of both O VI 5291 Å emission, and considerably broadened O V and C IV lines. For the remainder of our spectra the contribution of this star has been subtracted.

3.2. *Extinction variations*

The combined Hα/Hβ ratio and Whitford reddening curve enable us to determine the overall and, where relevant, variation of extinction within PN; the application of this procedure to NGC 6905 is illustrated in Fig. 5. As a result it is clear that, for the central region at least, there is some evidence to support a small increase in extinction towards the south – a variation in extinction of $\Delta m = 1$ mag appears to be superimposed upon a mean value $A_v = 2.9 \pm 0.1$ mag. If this is confirmed (and there seem few reasons to doubt this result), then we must suppose NGC 6905 to represent one of the few nebulae to be associated with intrinsic (i.e. local) extinction. This may also have a bearing upon our later model for the source, in which we propose the presence of a substantial exterior halo.

S/N ratios in the fainter outer lobes are necessarily worse, although we have summed a total of sixteen pixels for each data

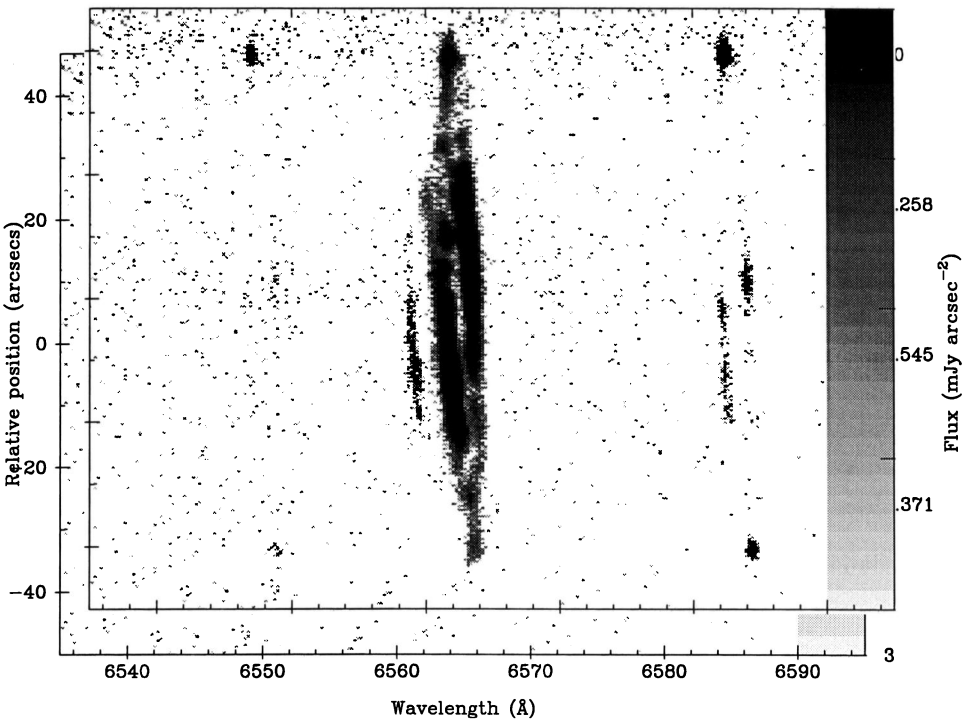

Fig. 2. Grey scale representation of the high resolution spectrum for NGC 6905, where the slit was oriented along the nebular major axis. [N II] emission is seen to be relatively strongly enhanced at the ansae, compared to Hα. Similarly, it may be noted that all of the lines are well resolved, and show evidence of tilting

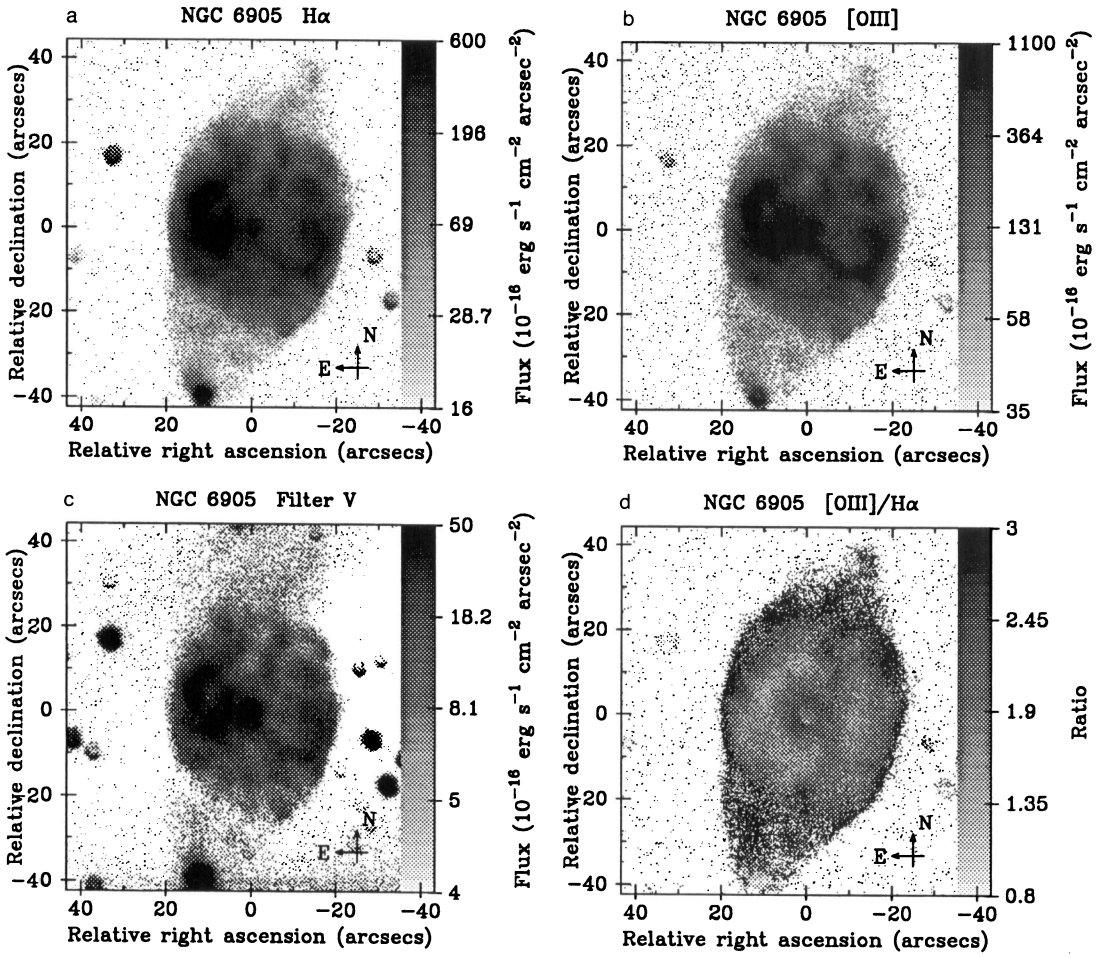

Fig. 3a–d. Composite of four images of NGC 6905, corresponding to **a** Hα, **b** [O III], **c** *V* and **d** Hα/[O III]

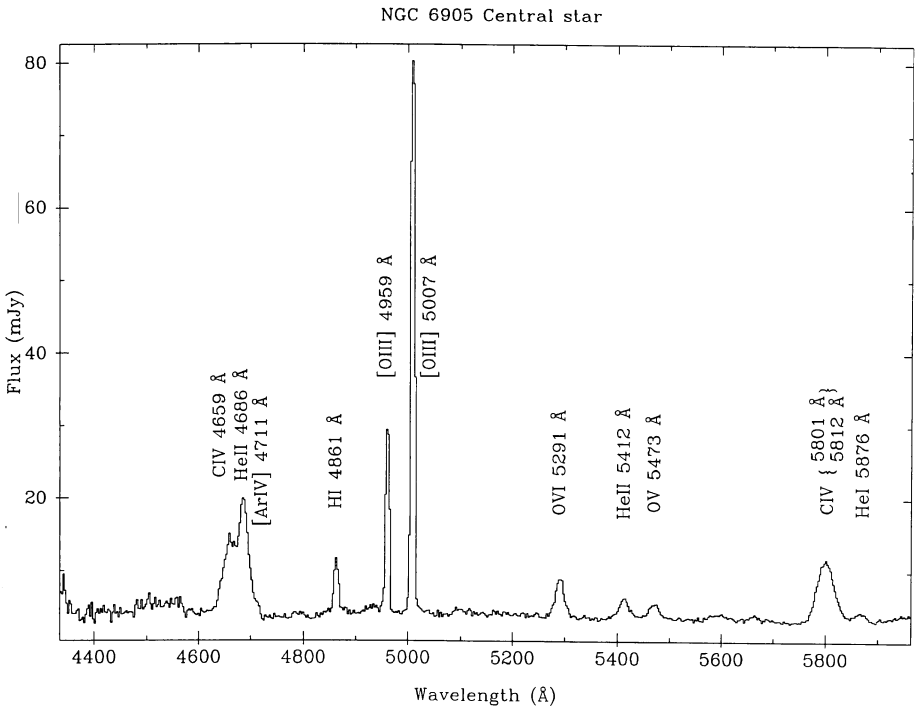

Fig. 4. Spectrum of the central star, showing clear Wolf-Rayet O VI sequence characteristics; note in particular the O VI 5291 Å line, and the very broad lines of O V and C IV

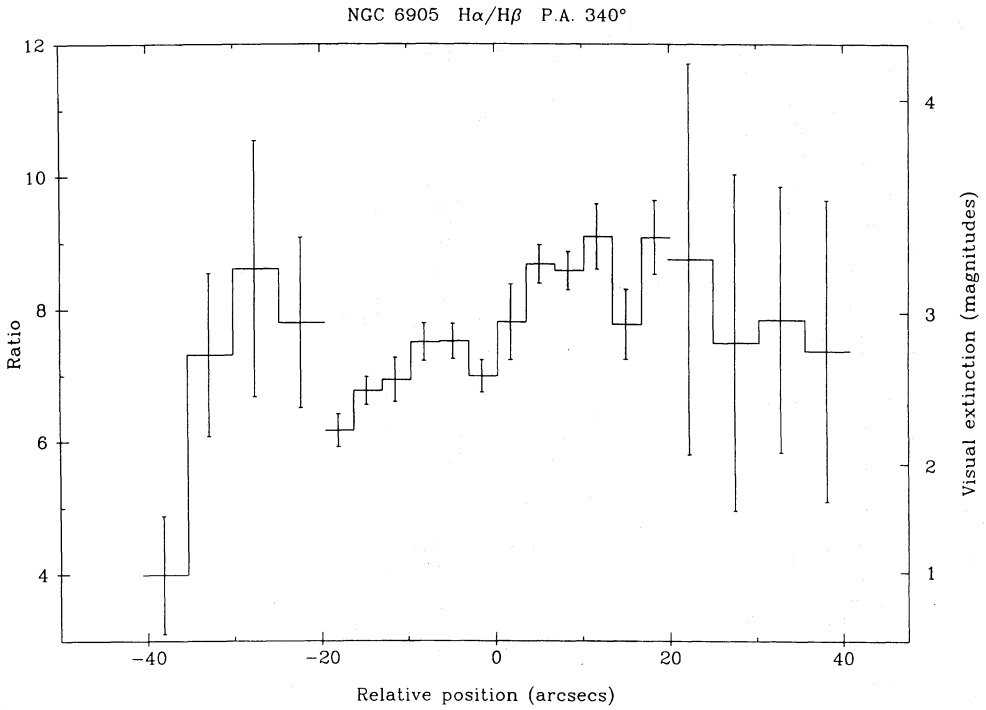

Fig. 5. Variation of extinction along the nebular major axis, where values correspond to an average over every ten pixels for the inner shell, and every sixteen pixels for the conical extensions. Note that the signal/noise for the exterior lobes is particularly poor, and any variation in extinction is correspondingly unclear

point in an attempt to alleviate this trend. Nevertheless, our results suggest values of A_v which are not appreciably different from the nucleus.

3.3. *Kinematic study*

Position-velocity maps derived from the high resolution Hα spectra are illustrated in Fig. 6, corresponding to the six traverses through the nucleus noted in Sect. 2.1; where it may be noted that negative positional displacements correspond to low pixel numbers (i.e. to easterly offsets from the nucleus where $0° \leqq \mathrm{PA} \leqq 180°$, and westerly offsets for $180° < \mathrm{PA} < 360°$). In all cases, there is a clear separation into an approaching and receding component. Except for a PA of 70° (which corresponds to the position of the minor axis) the envelope appears also to be tilted, suggesting an inclination of the nebula with respect to the line-of-sight. This inclination is maximum for a PA of 340°, corresponding to the major axis of the nebula.

Interpreting these dual components respectively as emission from the front and rear faces of an ellipsoidal shell, we have interpolated between our observations to obtain two-dimensional velocity maps for the front and back faces (Fig. 7a). A third velocity map, also included in Fig. 7a, corresponds to the velocity difference between the two shells.

In provisionally interpreting these results, we have constructed a simple two-component model of the nebula based on its observed physical appearance: we suppose the nebula to consist of a prolate spheroidal interior envelope with conical extensions, and a major axis tilted relative to the line-of-sight (Fig. 8). The trend of PN expansion velocities with nebular radius is by no means clear for sources taken generally, although the variation of expansion velocity with excitation species (Wilson 1950), and over the surface of non-spherical shells (Weedman 1968; Wilson 1958) appears broadly consistent with a proportionality between velocity and radius; we shall make this initial assumption for the present nebula.

Given such a model, it is then readily demonstrated that for the inner spheroidal nebular envelope:

$$b = -V_{\mathrm{Ea}} R_{\mathrm{Eb}} \sqrt{\frac{a^2 - R_{\mathrm{Eb}}^2}{V_{\mathrm{Eb}}^2 a^2 + a^2 V_{\mathrm{Ea}}^2 - R_{\mathrm{Eb}}^2 V_{\mathrm{Ea}}^2}}, \tag{1}$$

$$\sin^2 \theta_s = \frac{V_{\mathrm{Eb}}^2 - a^2}{b^2 - a^2}, \tag{2}$$

where b is the major axis of ellipsoid; V_{Ea} and V_{Eb} are the model velocities corresponding at the minimum and maximum projected radii; R_{Eb} is the maximum projected nebular radius, a is the minor axis of ellipsoid, and θ_s is the inclination of nebular axis to the line-of-sight.

The proportionality factor between velocity and radius is given through $F_e = -V_{\mathrm{Ea}} R_{\mathrm{Eb}}/ab$, for which case velocity along the major axis of ellipsoid varies as $V_b = F_e b$. For the conical outflow lobes, on the other hand, the methodology is more simple, and the maximum projected radius is given simply though $R_{\mathrm{Ebc}} = b_c \sin\theta_s$; where b_c is the length of the cone, and we suppose the minimum radius a_c of the cone to be the same as that of the ellipsoid.

Using this simple model, we have created three two-dimensional velocity maps for direct comparison with our observed results (Fig. 7b). As a result, it is clear that such relatively straightforward modeling permits an excellent variations within the exterior lobes are necessarily less obvious.

On the other hand, in fitting these results it has proved necessary to adopt a smaller proportionality factor for the velocity law in the cone, $F_c = V_{\mathrm{Ebc}} \cos\theta_s / b_c$ (where V_{Ebc} is the observed velocity at the tip of the cone relative to the central star), than in the case of the interior shell. Broadly speaking, ratios V/R for the lobes are approximately half those in interior shell, and it is clear that the kinematic properties of these regions are required to differ appreciably.

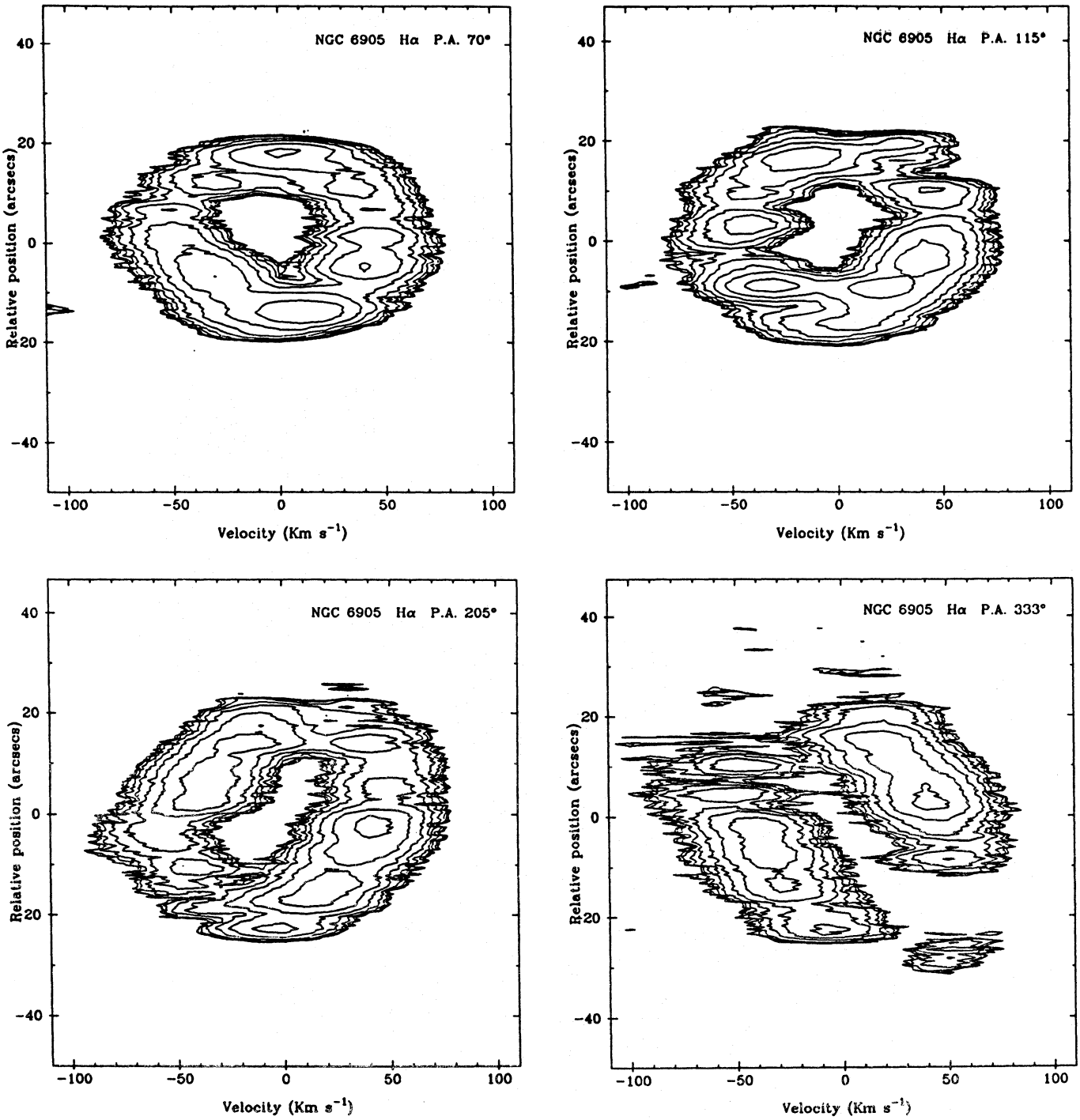

Fig. 6. Position-velocity maps in Hα for six slit orientations. Note the presence of more extended lobal emission close to PA 340°

Finally, the best match presented in Fig. 7b enables us to estimate a major axis inclination angle $131 \pm 4°$. The dimensions of the nebula, assuming a distance of 1800 pc (Maciel 1984), are 0.19 ± 0.01 pc and 0.135 ± 0.004 pc for the major and minor axis respectively, and 0.47 ± 0.03 pc for the length of the conical extensions; the velocity proportionality factor in the ellipsoid is $310 \pm 10\,\mathrm{km\,s^{-1}\,pc^{-1}}$, and $147 \pm 2\,\mathrm{km\,s^{-1}\,pc^{-1}}$ for the exterior shell.

4. The exterior shell and the ansae

One of the most intersting aspects of our spectra is the presence of ansae at the extremities of the major axis, as illustrated in Fig. 2. In our high resolution spectrum taken along the major axis of nebula, these ansae appear particularly intense in [N II], although the enhancement in Hα is significantly smaller; a trend which suggests that the ansae are nitrogen enriched or that low excitation

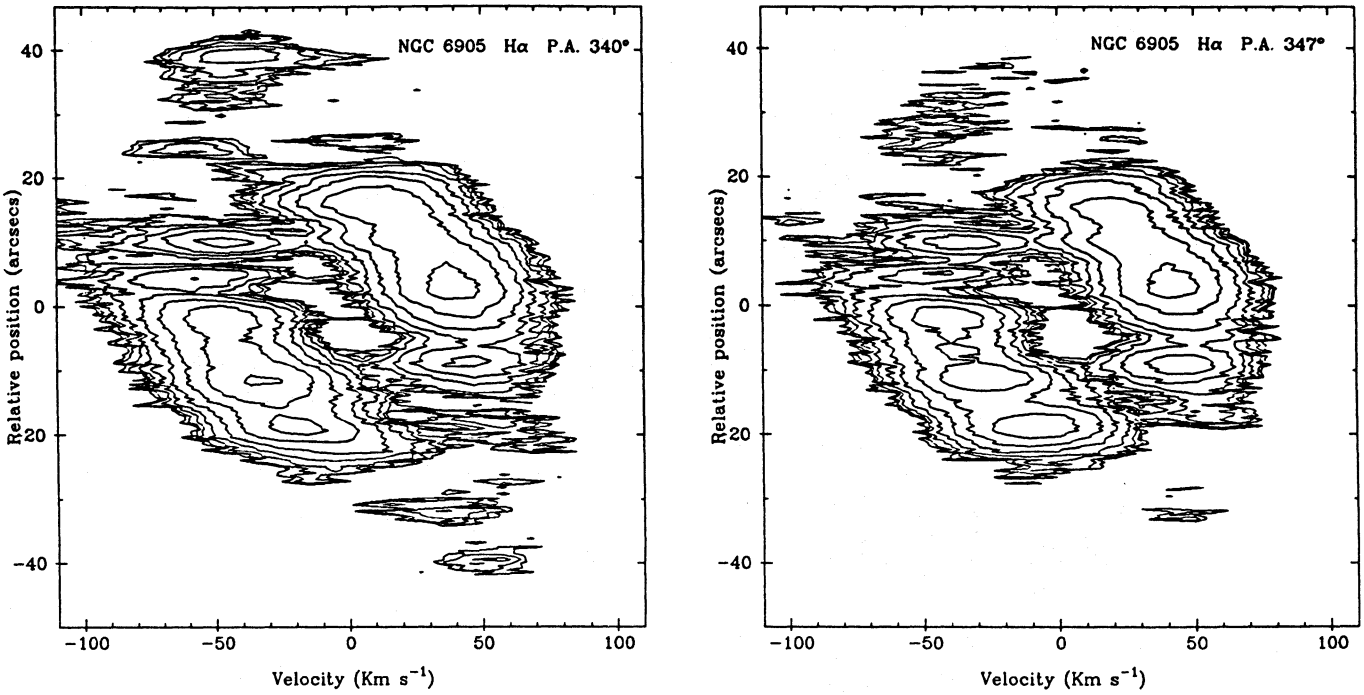

Fig. 6 (continued)

species are preferentially enhanced through collisional excitation. To illustrate this effect more clearly, we have determined the spatial variation in the ratio [N II] λ6584/Hα illustrated in Fig. 9; the ansae and the exterior shell show up as regions of extremely strong [N II] emission, whilst the interior shell is characterised by very much lower values of [N II]/Hα. Similar (velocity unresolved) trends are also derived from our lower resolution spectra (Fig. 10) where the horizontal axis corresponds to distance along the major axis, and the ratio again increases rapidly towards the ansae.

The variation of line intensity with relative position is shown for eight differing transitions in Fig. 11: [N II] 6584 Å, Hα 6563 Å, [S III] 6312 Å, He I 5875 Å, He II 5412 Å, [O III] 5007 Å, Hβ 4861 Å and He II 4686 Å. Note the strong peaking in [N II] at the southerly ansa, and a very much weaker maximum towards the north. Also, the emission for the inner shell appears quite similar for Hα, [O III] and Hβ, and (excepting the central maximum) for He II as well, with evidence for several distinct emission components. Finally, there is evidence for enhanced He I emission near the southern ansa, by an amount which would be rather unexpected were these trends reflective of stratification effects alone.

In addition to this spectral data, our direct images of the nebula in Hα and [O III] reveal both northern and southern ansae (the latter obscured by a field star) and the fainter exterior shell. We have also divided the [O III] and Hα results to obtain the quotient image in panel 4. Although the ansae are not particularly strong, it is clear from this latter image that the ratio [O III]/Hα is generally higher for the faint nebular extensions, and the exterior part of the bright inner shell, and very much smaller over most of the interior nebular shell. In addition, the [N II] image of Balick (1987) shows that the ansae are clearly very much stronger than nearby nebular emission.

In summary, the conical extensions have an interesting set of characteristics:

(a) they generally have higher values of [N II]/Hα, with particularly strong [N II] (and possibly He I) emission in the ansae,

(b) they appear to have a different set of kinematics from the interior shell, and are clearly not part of the same expansion process (assuming, of course, that our model in Fig. 7b is correct, and the conical extensions are symmetrically disposed about the central ellipsoid),

(c) they have comparatively high levels of [O III]/Hα,

(d) there is no evidence for limb brightening, such as might be expected for a hollow shell configuration, and

(e) there is not much evidence to favour peaking of emission towards the major axis, such as might be expected for a shell which is uniformly filled.

To explain these characteristics, as well as the rather peculiar spatial morphology of this source, we propose the model outlined in Fig. 12 (based, in turn, upon the shock outflow modeling of Cantó (1980) and Barral & Cantó (1981)). In this case, the conical extensions are presumed to arise from shock interaction between an outflowing wind and the confining (possibly neutral) gas; for which case the post-shock zone is expected to be reasonably thin, and unresolved by our present observations. As a consequence, limb brightening effects (towards the projected edges of the conical zone) would be expected to be small, providing the projected width of the shock is significantly less than the seeing. A further consequence of such a shock is that we would expect various low excitation species to be enhanced, including [N II], whilst (as we shall see) the shock interface between wind and halo would be expected to lead to similar conical morphologies; a conclusion which holds for broad range of parametric assumptions.

Finally, shock refraction of this wind may lead to focussing of material at the tip of the outflow cone, and particularly severe shock activity, intense low excitation emission, and high densities. This is precisely the location of the low excitation ansae, and provides a natural explanation for these otherwise enigmatic features.

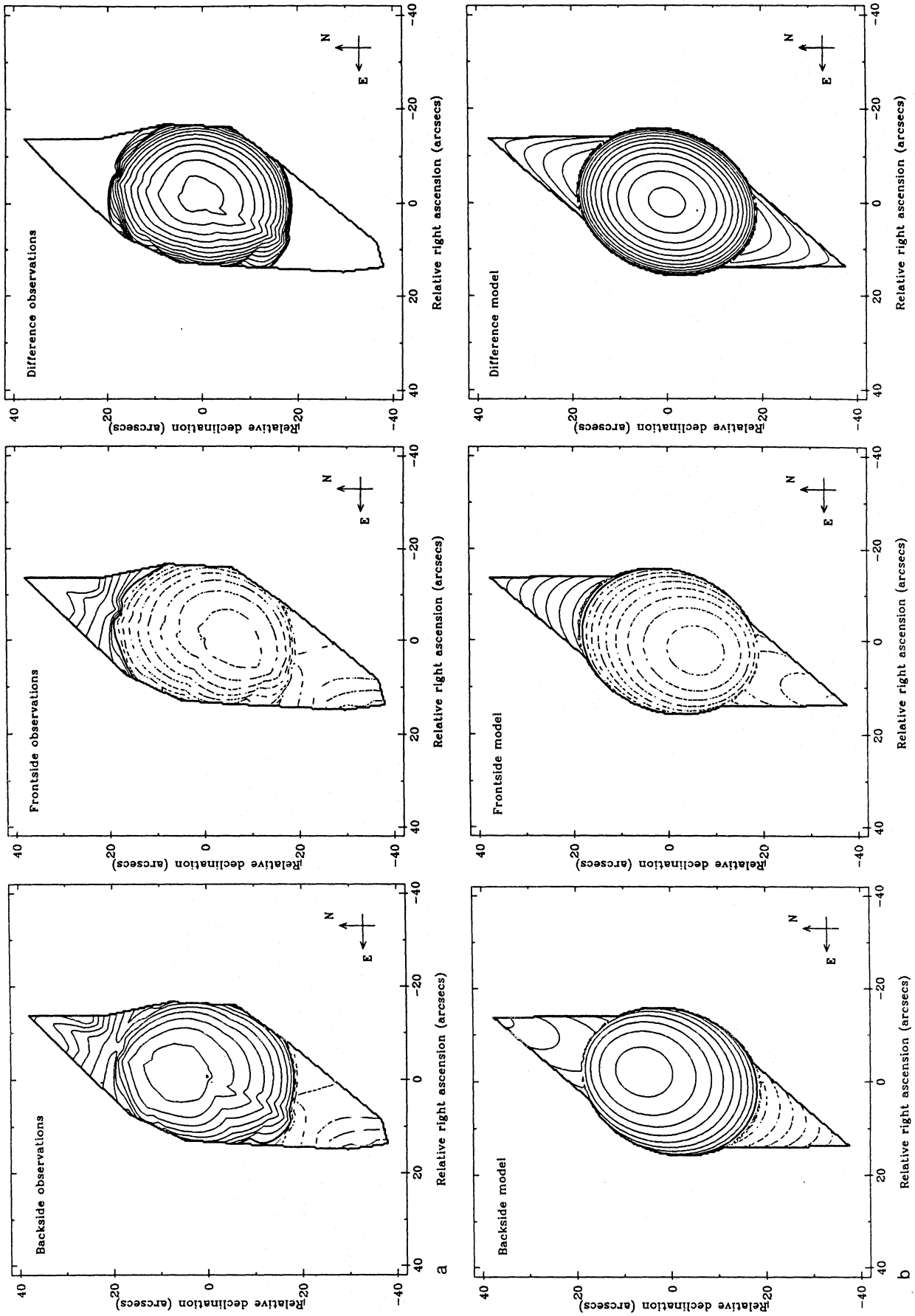

Fig. 7a and b. Two-dimensional velocity maps deriving from **a** observation, and **b** a simple model of the source. Negative velocities are represented by dashed lines, positive velocities by solid lines, whilst zero velocity is in all cases indicated by the broader solid lines. Contours are scaled linearly from − 48 to 48 km s^{-1} for the rear and front sides of the nebula, and from 0 to 98 km s^{-1} for the velocity difference map

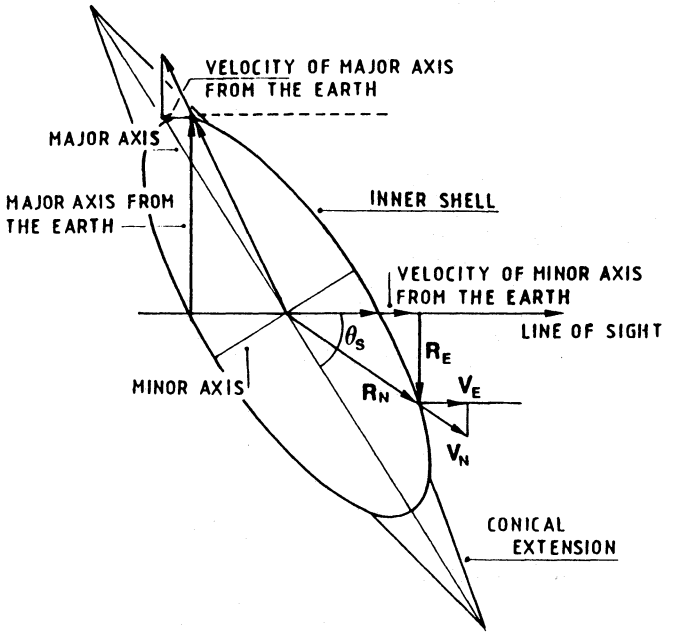

Fig. 8. Simple kinematic model for NGC 6905; used in replicating the velocity trends in Fig. 7. We assume that velocity is proportional to radius, and that the lobes lie along an extension of the interior major axis; an assumption which leads to reasonable results providing the ratio V/R differs between lobes and spheroid

5. A physical model for NGC 6905

In modeling the exterior outflow lobes in terms of a shock structure, we shall be assuming that the velocity of stellar wind is orders of magnitude greater than the expansion velocity of the halo; a presumption which is consistent with trends observed in other PN, enables us to approximate the outflow in terms of pseudostationary shocks, and (as we shall see) leads to reasonably self-consistent solutions. Such a presumption also applies to the related analyses of NGC 6302 (Silvestro & Roberto 1987) and other comparable sources (Barral & Cantó 1981), in which similar shock models are employed to explain the bilobal morphologies of type I nebuale. The principal emission regime is assumed to be located in relatively cool post-shock zones, well downstream of the primary shock front (cf. Cantó 1980). In consequence, components of velocity normal to the shock surface are expected to be low, and the observed kinematics dominated by shock-refracted tangential flows.

A secondary assumption implicit in this analysis is that the interior contact discontinuity (between shocked and stellar winds) is tolerably close to the external edge of the nebula. Given high wind velocities (see later), this in turn suggests a period of cavity evacuation and subsequent pseudo-stability which is relatively short-lived and of order perhaps $\sim$ few 10^2 yr or less; any very much longer periods would likely lead to rapid enhancement of the shocked-wind règime, and dominance of shell kinematics by an internal bubble of hot gas. Over time, this would in turn lead to a smoothing out of the structures to be discussed below, and a trend to spheroidal shells characteristic of most main-stream PN.

Finally, previous detailed applications of such models have invoked an interaction between outflowing winds and homogeneous media, or media characterised by one-dimensional density variations. In the present case, we will suppose (more realistically) that the outflowing wind interacts with a halo possessing a radial density variation; previous discussions have been generalized to allow for this more realistic treatment.

Given these conditions, we are interested in establishing the viability of such shock models in explaining the source morphology, kinematics, and surface brightness variation; and the likelihood that such features can be generated through a reasonable combination of wind velocities and mass-loss rates. Such models as are considered here cannot, of course, be regarded as definitive; there are too many uncertainties concerning basic

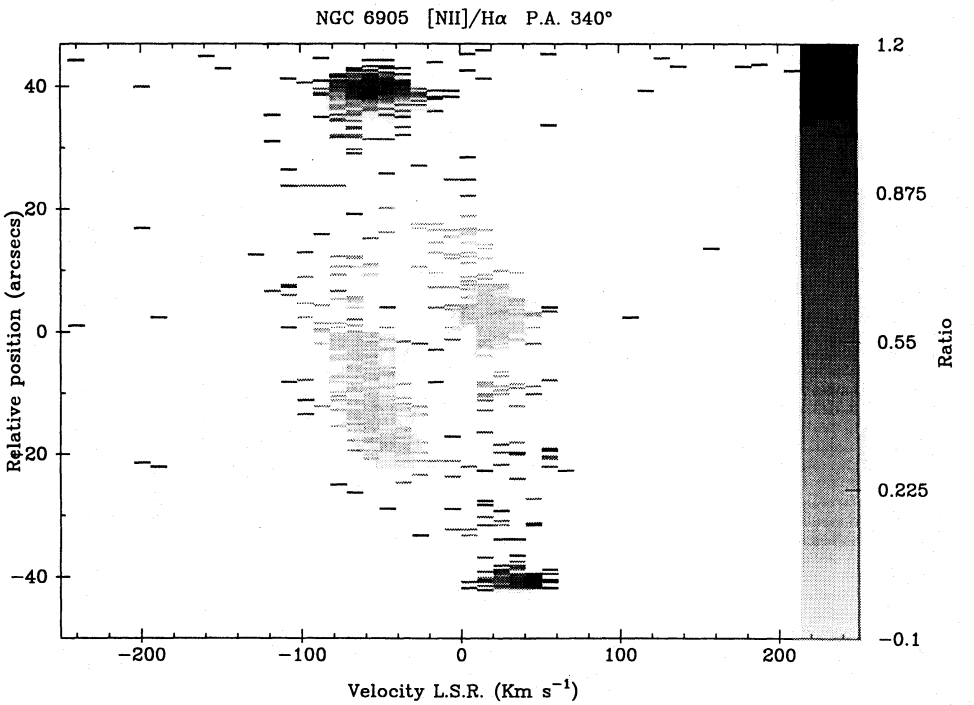

Fig. 9. Grey scale representation of the ratio between our high resolution Hα and [N II] lines, corresponding to a slit position along the nebular major axis. Note the enhanced ratio values close to the ansae

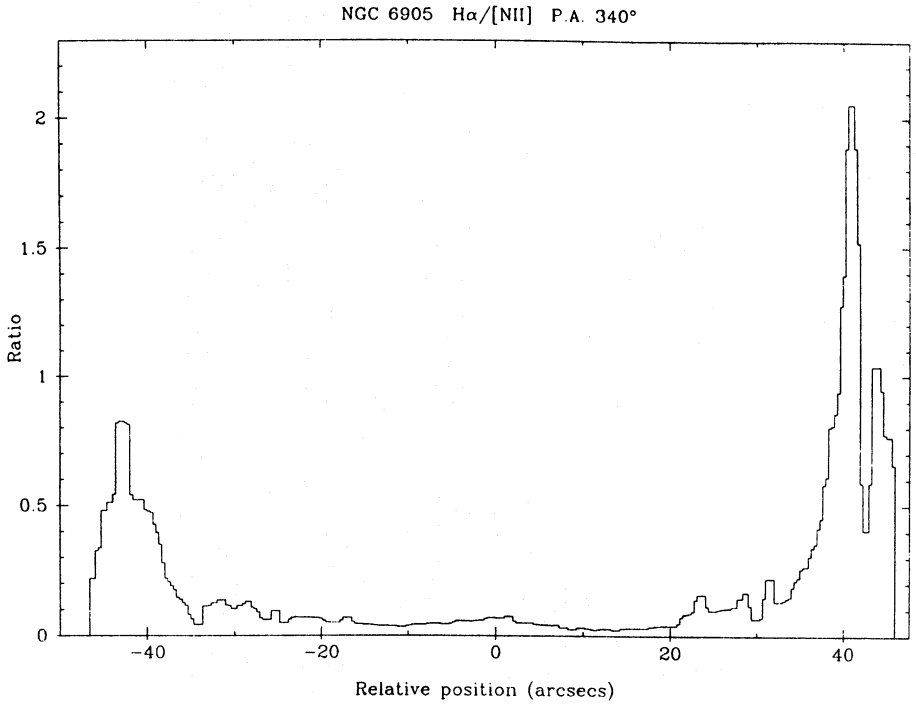

Fig. 10. Major axis variation in the ratio between Hα and [N II], the results in this case deriving from our low resolution spectrum

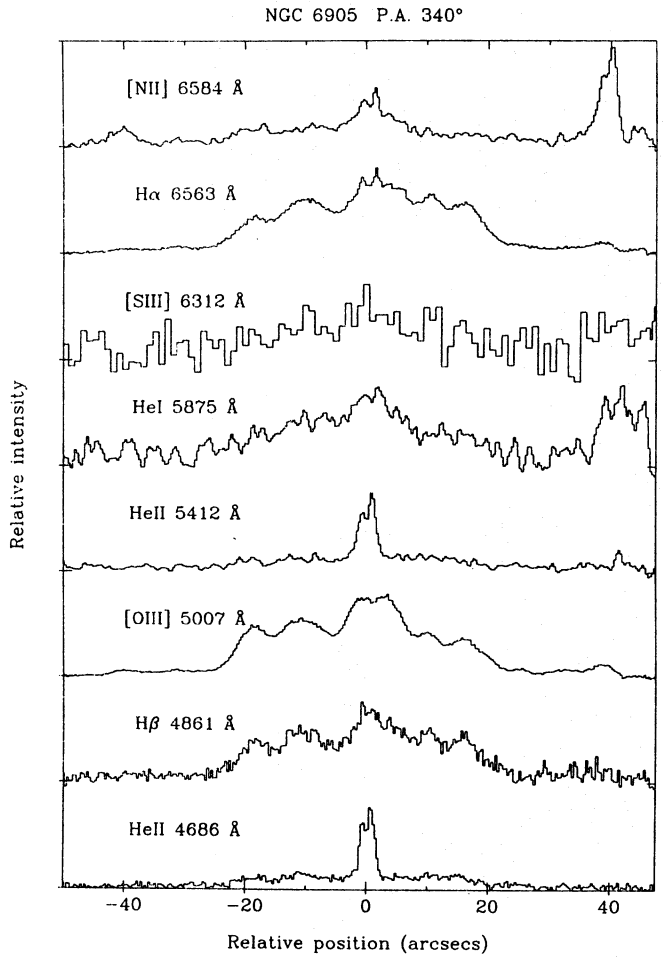

Fig. 11. Composite emission variation of several lines along the nebular major axis, deriving from our low resolution spectra. Note again the relatively higher [N II] emission at the ansae

source properties. We aim, however, to show that these models are at least plausible – and possibly unique – in explaining such a wide variety of source characteristics.

To this end, therefore, we consider the model illustrated in Fig. 12, in which the nucleus of the PN is immersed in a cloud of density ϱ, uniform temperature T, and constant sound speed c. This figure shows the non-spherical static flow configuration created through the interaction of an isotrophic stellar wind with the surroundings, resulting in two cavities symmetrically placed about the central star. The flow is bounded by a shock in the wind as described by Cantó (1980) and Barral & Cantó (1981).

The pressure balance determining the locus of the shock surface is then given through:

$$P_s = \varrho_w V_{\star\perp}^2 + \Delta_{CE}, \tag{3}$$

where P_s is the pressure of the ambient medium exterior to the shock, ϱ_w is the wind density at the shock, $V_{\star\perp}$ is the normal component of the wind velocity with respect to the shock surface, and Δ_{CE} is the centrifugal correction. Under these circumstances, if the density in the cloud is represented by $\varrho(R,\theta) = \varrho_\star f(R,\theta)$, where $\varrho_\star$ is density at the position of the star (prior to interaction with the stellar wind), then the equation of hydrostatical equilibrium will be given through (Cantó 1980)

$$f(r\cos\theta) = \frac{1}{(r^2+r'^2)} \left[1 + \frac{r^2+2r'^2-rr''}{\sqrt{r^2+r'^2}} \frac{1}{r\sin\theta} \int_{\theta_0}^{\theta} \frac{r'}{\sqrt{r^2+r'^2}} \sin\theta \, d\theta\right], \tag{4}$$

where $r \equiv R/R_0$, and $R_0 \equiv \sqrt{\dot{M}_\star V_\star / 4\pi c^2 \varrho_\star}$ is the radius of the shock at $\theta = \pi/2$. $\dot{M}_\star$ is the mass-loss rate for the wind, and $V_\star$ is the wind velocity.

In addition to the continuous enveloping halo, presumably a remanent of the superwind ejection phase, it is also necessary to

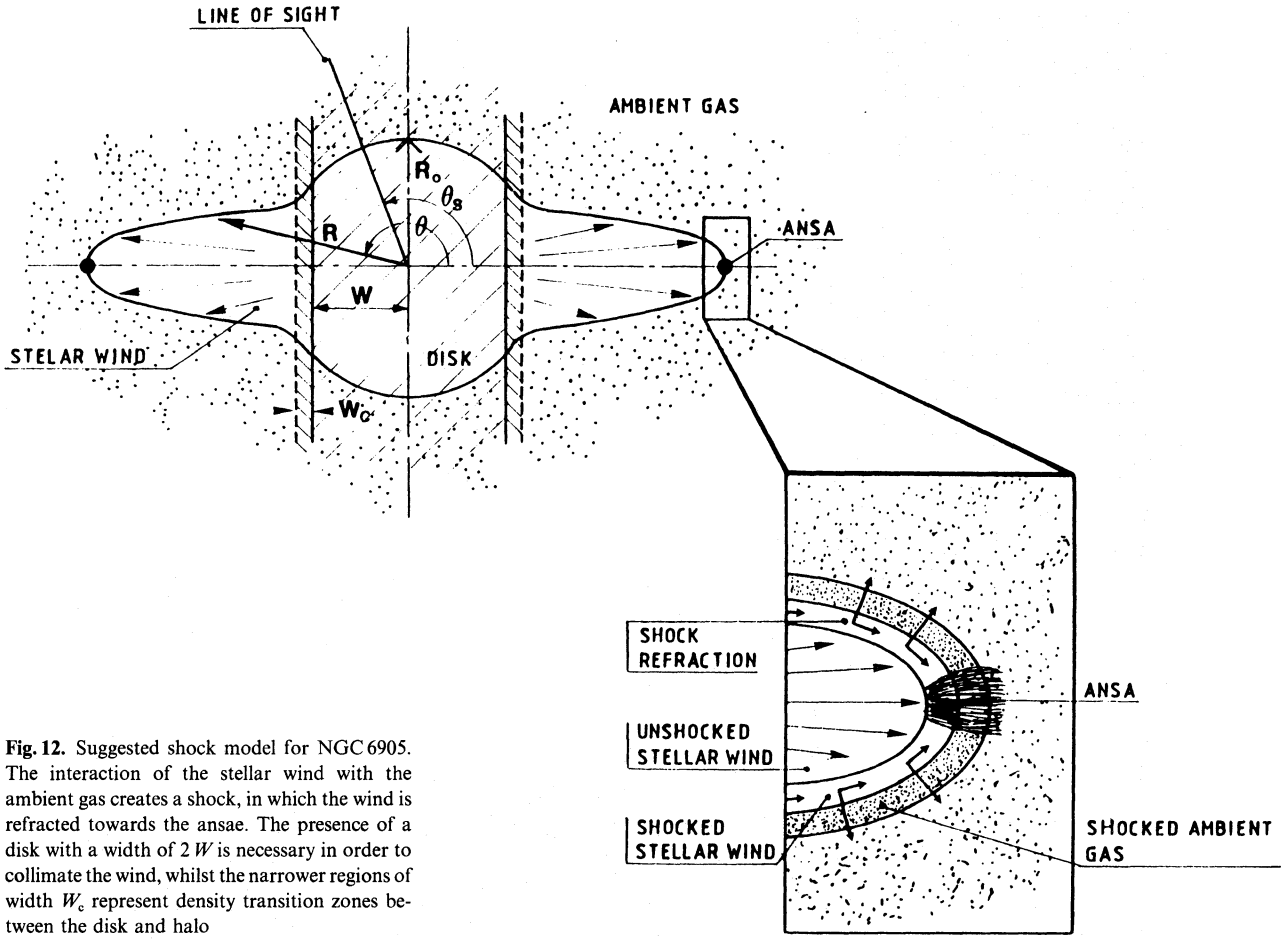

Fig. 12. Suggested shock model for NGC 6905. The interaction of the stellar wind with the ambient gas creates a shock, in which the wind is refracted towards the ansae. The presence of a disk with a width of $2W$ is necessary in order to collimate the wind, whilst the narrower regions of width W_c represent density transition zones between the disk and halo

assume an inner discoidal region of higher densities; a type of structure for which we have preliminary evidence in PN molecular outflows (e.g. Phillips et al. 1991), and a variety of type I bilobal nebulae (e.g. Phillips 1990). Such an assumption enables us to model the source as one of two types of structure. In the first of these cases, we many presume that the region of shock interaction (and present modeling) is relevant for the exterior lobes alone; that the wind is collimated by an interior ionized shell, and escapes through openings in this shell to interact with the external medium. Under these circumstances, the contribution of shock refraction at small radii (interior to the lobes) to the observed structure at larger radii is regarded as negligible – and this in turn can be simulated by assuming a constant density within the collimating disc (whence $\Delta_{CE} = 0$). For this case, the shock surface within the inner disc is spherical, and is *not* to be compared with the observed nebular structure.

This is the model we favour here.

In the second case, we assume that the entire nebular boundary and morphology is defined by the shock interface between the outflowing wind and the enveloping halo/disc; in which case, it should be possible to model not only the exterior conical lobes, but also the interior (higher luminosity) spheroidal zone. This is almost certainly less realistic – it takes no account of photoionization, for instance – although we shall nevertheless again find that such models replicate the observed structure reasonably well, providing densities within the collimating disc are permitted to vary. Hereafter, we refer to the model with a disc of constant density as CDDM, and the model with the disc having non-constant density as NCDDM.

Finally, it is analytically convenient to assume a continuous variation in density between the disc and halo; discontinuous variations in density head to breakdowns in our iterative procedures. Such a presumption would also seem plausible for most realistic outflow models; although in the present case, the width W_c of the transition is assumed to be small, and the regime has little influence upon derived shock properties.

In detail, therefore, we have developed a form of density law which enables us to explore a wide range of models, and yields robust solutions over a broad range of parameters. The density *within* the disc is allowed to vary as a Gaussian, whilst densities outside of the disc change as $R^{-\alpha}$, with α varying between 0 and 3. Finally, densities within the transition zone are again required to follow a Gaussian distribution, of variable width $W_c/\ln(Br^\alpha/A)$. Taking R, θ, W and W_c to be defined as in Fig. 12, and defining $r \equiv R/R_0$, the general density then varies as

$$f(r,\theta) = \begin{cases} \dfrac{A}{r^\alpha} & \text{if} \quad R_0|r\cos\theta| \geqq W + W_c; \\ B\exp\left\{-\ln\left(\dfrac{Br^\alpha}{A}\right)\left(\dfrac{|r\cos\theta| - W}{W_c}\right)^2\right\} & \text{if} \quad W + W_c > R_0|r\cos\theta| \geqq W; \\ \exp\left\{-\ln\left(\dfrac{1}{B}\right)\left(\dfrac{r\cos\theta}{W}\right)^2\right\} & \text{if} \quad W > R_0|r\cos\theta|, \end{cases} \tag{5}$$

Table 1. Summary of parameters for NGC 6905 shock models

α	A	B	W	W_c	R_0	Comments
0	0.218	1	0.78	0.05	20 ± 1	Constant
1	0.412	1	0.78	0.05	20 ± 1	disk
2	0.711	1	0.78	0.05	20 ± 1	
3	1.15	1	0.78	0.05	20 ± 1	
0	0.151	0.48	1	0.05	15.5 ± 0.5	Semi-constant
1	0.266	0.48	1	0.05	15.5 ± 0.5	disk
2	0.441	0.48	1	0.05	15.5 ± 0.5	
3	0.697	0.48	1	0.05	15.5 ± 0.5	

where A and B are constants (see below). Note that for the CDDM, B is taken as unity, and the disk density is then constant and equal to 1.

The integration of Eq. (4) is taken to commence at $\theta_0 = \pi/2$, where boundary conditions are defined by Barral & Cantó (1981). In the present case we also have $r_0'' = (\sqrt{1 - 24\ln(B)/W^2} - 1)/6$, since the second derivative of f with respect to $(r\cos\theta)$ at $\theta = \pi/2$ is $f_0'' = 2\ln(B)/W^2$.

As a result, in the CDDM, as for the NCDDM, the values of B will be closely the same; unity for the CDDM, and very close to unity for the NCDDM. The values of A, B, W and W_c for which we obtain our best results are given in Table 1, as a consequence of which we obtain the CDDM profiles in Fig. 13a, and the NCDDM profiles in Fig. 13b; wherein we also illustrate differing α-values, and superimpose our present [O III] image. Although there are few differences between these curves, the best fit solutions suggest $\alpha = 2\pm1$ for the CDDM, and $\alpha = 0\pm1$ for the NCDDM.

Using the momentum flux parallel to the shock, and the flux of mass crossing the shock surface (see Cantó 1980), the velocity of the flow is given through

$$V_t = -V_\star \frac{1}{\cos\theta} \int_{\theta_0}^{\theta} \frac{r' \sin\theta}{\sqrt{r^2 + r'^2}} \mathrm{d}\theta, \tag{6}$$

where, as noted earlier, we presume velocity vectors to be tangential to the shock surface. If θ_s is the inclination to line-of-sight of the symmetry axis of shock (Fig. 12) the observed velocity will then be given by:

$$V_r = -V_t \left[\frac{r' \cos(\theta+\theta_s) - r \sin(\theta+\theta_s)}{\sqrt{r^2 + r'^2}} \right]. \tag{7}$$

Equally, the intrinsic brightness of the shock surface is given by the rate at which kinetic energy is thermalized in the shock front

$$L_s = L_0 \frac{r}{\sqrt{(r^2 + r'^2)^3}}, \tag{8}$$

where L_0 is the intrinsic brightness at $\theta = \pi/2$: $L_0 = \dot{M}_\star V_\star^2 / 8\pi R_0^2$. As a result, the observed brightness is given through

$$L_r = \frac{L_s}{L_0} \mathrm{e}^{-\tau}, \tag{9}$$

where τ is the line-of-sight extinction (taken here to broadly invariant – although see also the discussion in Sect. 3.2).

Given these expressions, the variation of velocity and brightness as a function of α and radius is illustrated in Fig. 14a for the CDDM, and in Fig. 14b for the NCDDM. Superimposed on these, the error bars correspond to velocity trends derived from our present results – whence the fit, within (the substantial) error uncertainty, is seen to be reasonably good in both cases. Clearly it would be invidious to choose one model over another, although it is apparent that model velocity trends are in both cases plausible.

The variation of luminosity with lobe radius is reasonably gentle – qualitatively similar to the emission trends observed

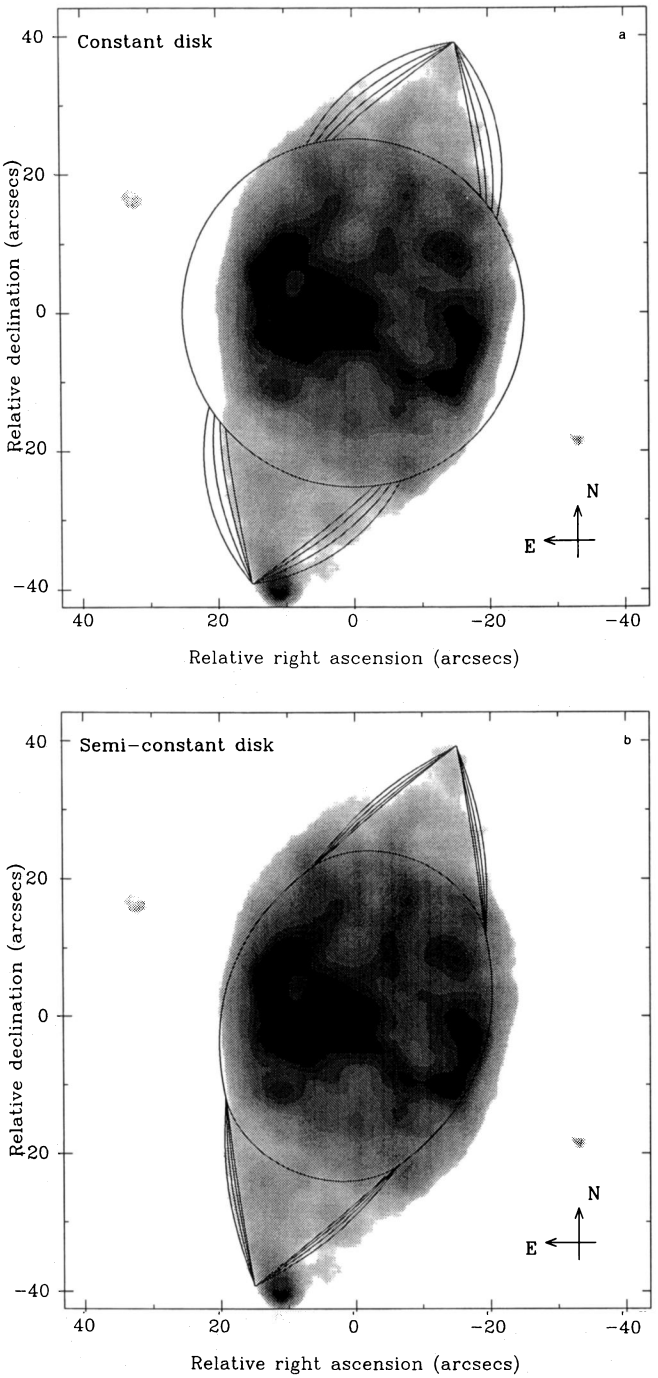

Fig. 13a and b. Solutions of the shock model for NGC 6905 superimposed upon a grey scale image of the nebula, where we illustrate cases where **a** the disc density is constant (CDDM) and **b** the disc density is variable (NCDDM) (see text). In each case α is allowed to vary from 0 (exterior curves) through to 3

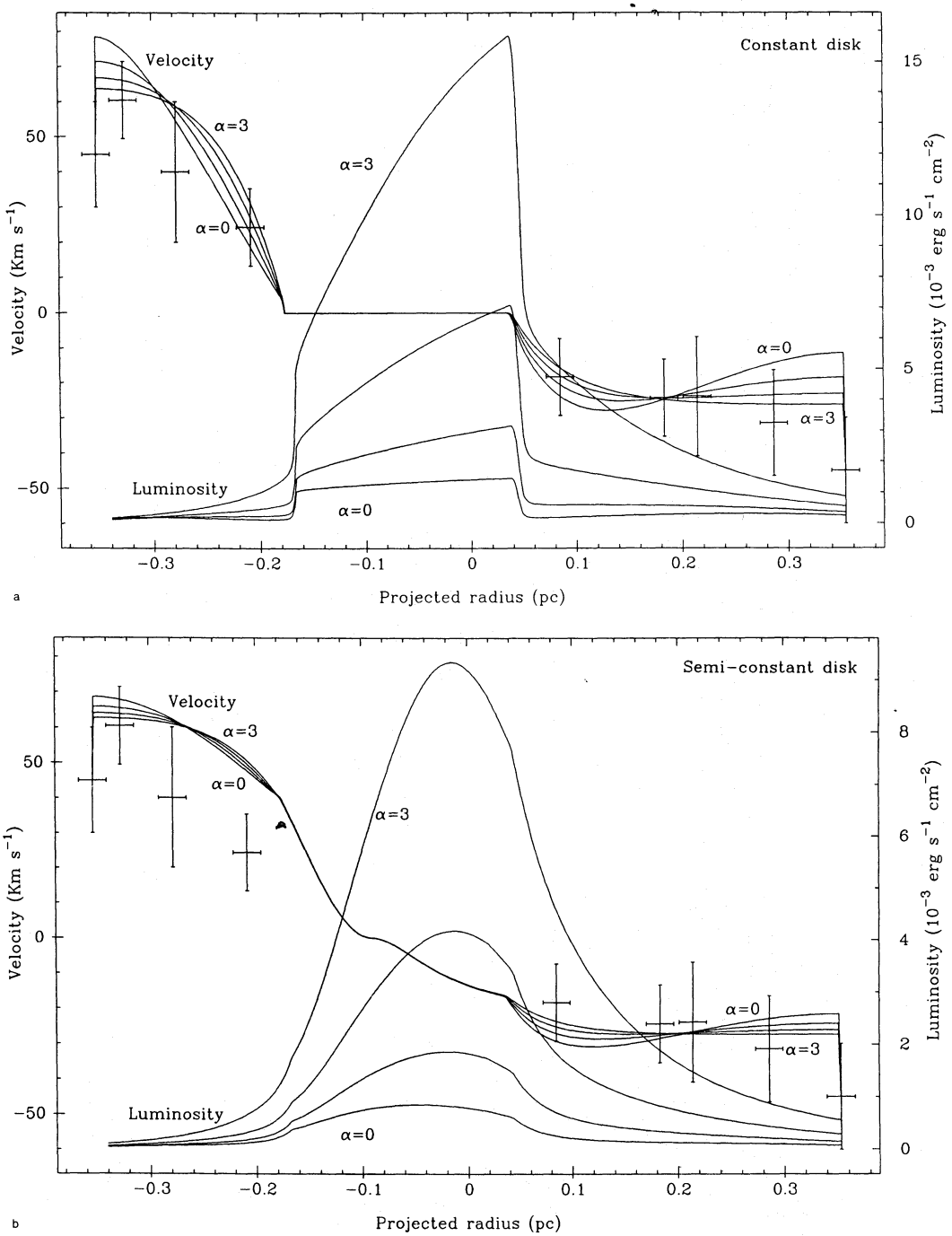

Fig. 14a and b. Variation of (i) line-of-sight model velocities in the nearest shock surface, and (ii) the line-of-sight model integrated brightness, versus projected source radius. Superimposed are error bars corresponding to observed major axis velocities in the exterior conical emission lobes. The fit between our observed and model velocity trends appears reasonably satisfactory for **a** the CDDM having $\alpha = 2$, but somewhat less so for **b** the NCDDM

here (although direct comparisons would of course be difficult, and complicated by uncertainties in density and temperatures within the post shock emission zone). Similarly, the models suggest a gross discrepancy between emission in the lobes, and the luminosity of the core – of similar order to that observed in various of the emission lines. Broadly speaking, therefore, it is clear that however the source is interpreted – a shock envelope defined solely by the interaction of wind and halo, or a shocked lobal structure with interior, photoionized ellipsoidal shell – the present models show promise in explaining the source morphology, surface brightness variation, kinematics, the location and emission characteristics of the ansae, and (in all likelihood) the spatial trends in line ratios.

Given that such models provide a reasonable description of the source, therefore, we may proceed further to deduce parameters such as wind velocity and mass loss rate; parameters which, as it turns out, are reasonably independent of the uncertainties and assumptions in source physical characteristics.

Table 2. Derived physical characteristics for the NGC 6905 shock models

α	$V_\star$ (km s^{-1})	$\dot{M}_\star$ [a] (10^{-7}) ($M_\odot$ yr^{-1})	L_0 [a] (10^{-3}) (erg s^{-1} cm^{-2})	$\varrho_\star$ (10^{-20}) (g cm^{-3})	n_{ec} [a] (10^{-3}) (cm^{-3})	n_{e0} [a] (10^{-3}) (cm^{-3})	Comments
0	1000 ± 100	0.40 ± 0.03	3.0 ± 0.3	0.917	0.5 ± 0.1	3 ± 1	Constant
1	900 ± 100	0.73 ± 0.05	5.3 ± 0.6	1.65	0.9 ± 0.2	70 ± 10	disk
2	900 ± 100	1.4 ± 0.1	11 ± 1	3.25	1.8 ± 0.4	13 ± 3	
3	1000 ± 100	2.9 ± 0.2	23 ± 3	6.89	3.6 ± 0.8	26 ± 6	
0	430 ± 50	0.73 ± 0.03	2.0 ± 0.2	1.32	2 ± 0.4	24 ± 5	Semi-constant
1	430 ± 50	1.44 ± 0.07	3.8 ± 0.4	2.58	4 ± 1	50 ± 10	disk
2	430 ± 50	3.0 ± 0.1	8 ± 1	5.33	8 ± 2	100 ± 20	
3	430 ± 50	6.5 ± 0.3	17 ± 2	11.6	18 ± 4	220 ± 50	

[a] Results should be multiplied by the $(T/10^2\,\mathrm{K})(n_\mathrm{H}/10^3\,\mathrm{cm}^{-3})$, where T and n_H correspond to halo temperatures and densities close to the nebular major axis limits.

Firstly, we note that the scaling ratio R_0 (defining the shock radius at $\theta = \pi/2$) may be assessed by comparing our models of the source, with the observed dimensions of the nebula. Thus in the NCDDM, R_0 corresponds to the size of minor axis, which is observed to be 0.135 ± 0.004 pc. However, in the CDDM the observed minor axis does not correspond with R_0, and it is therefore necessary to determine thus parameter by comparing observed and model major axis lengths; whence $R_0 = 0.18 \pm 0.01$ pc. Both of these values assume a distance of 1800 pc (Maciel 1984).

From our spectroscopic observations, the line-of-sight velocity at the northern extremity of the exterior shell is 45 ± 5 km s^{-1}; whence for the CDDM and $\alpha = 2$ we determine $V_r = 4.78\ 10^{-2}$ (Eqs. 6 and 7) together with a velocity $V_\star = 900 \pm 100$ km s^{-1} for the stellar wind. In the NCDDM, the predicted velocity of the model for $\alpha = 0$ is $V_r = 0.104$, and the velocity of the outflowing wind would then be $V_\star = 430 \pm 50$ km s^{-1}. Both velocities are of order of magnitude similar to those observed in other PN (e.g. Phillips 1984).

The preshock electron density $n_e(R)$ at radius R is related to the mass-loss rate through:

$$\dot{M}_\star = n_e 4\pi R^2 V_\star \bar{m} \qquad (11)$$

where $\bar{m} \simeq 2\ 10^{-24}$ gr is the average mass per particle.

From hydrostatical equilibrium we have $n_e \bar{m} V_\star^2 = c^2 \varrho$ for every point in the shock; and in particular, for the shock location at which $\theta = \theta_0$, where $R = R_0$, we have $\varrho = \varrho_\star$. If we assume a value for ϱ close to the tip of the shock of $n_\mathrm{H} = 10^3$ cm^{-3}, we can evaluate the initial density of ambient gas at the position of the star $\varrho_\star = n_\mathrm{H} \bar{m} f(R_0, \pi/2)/f(b_c, \pi)$; whence we obtain for the CDDM $(\alpha = 2)\,\varrho_\star = 3.25\ 10^{-20}\,(n_\mathrm{H}/10^3\,\mathrm{cm}^{-3})$ gr cm^{-3}, and for the NCDDM $(\alpha = 0)\,\varrho_\star = 1.32\ 10^{-20}(n_\mathrm{H}/10^3\,\mathrm{cm}^{-3})$ gr cm^{-3}. Equally, assuming a temperature of $T = 10^2$ K and using $c \equiv \sqrt{Tk/\bar{m}}$, where k is the Boltzmann constant, the isothermal sound speed in the ambient gas is $c = 0.83\ (T/10^2\,\mathrm{K})^{1/2}$ km s^{-1}. For $\alpha = 2$ in the CDDM we then find $n_{e0} = 1.3 \pm 0.3\ 10^{-2} F(T, n_\mathrm{H})$ cm^{-3}, where $F(T, n_\mathrm{H}) = (T/10^2\,\mathrm{K})\ (n_\mathrm{H}/10^3\,\mathrm{cm}^{-3})$, and for $\alpha = 0$ in the NCDDM we determine $n_{e0} = 2.4 \pm 0.5\ 10^{-2} F(T, n_\mathrm{H})$ cm^{-3}.

Another region of particular interest is the tip of shock. At this position $R = b_c$, and we obtain a density $n_{ec} = 1.8 \pm 0.4\ 10^{-3}\ F(T, n_\mathrm{H})$ cm^{-3} for the CDDM and $\alpha = 2$, and a value $n_{ec} = 2.0 \pm 0.4\ 10^{-3}\ F(T, n_\mathrm{H})$ cm^{-3} for the NCDDM and $\alpha = 0$. Finally, the corresponding values of mass-loss rate are: for the CDDM with $\alpha = 2$, $\dot{M}_\star = 1.4 \pm 0.1\ 10^{-7}\ F(T, n_\mathrm{H})\ M_\odot$ yr^{-1}, and for the NCDDM with $\alpha = 0$, $\dot{M}_\star = 7.3 \pm 0.3\ 10^{-8} F(T, n_\mathrm{H})\ M_\odot$ yr^{-1}. These values are presented in Table 2, together with estimates corresponding to other values of α.

It is seen in general, therefore, that mass-loss rates are again consistent with values estimated for other nebulae (e.g. Phillips 1984); and in particular match values pertaining in NGC 6543 (Castor et al. 1981) and NGC 7009 (Benvenuti & Perinotto 1980; Köppen & Wehrse 1980), a morphologically not dissimilar nebula.

Finally, given the above mass-loss rates, we may determine values of intrinsic brightness at the shock surface; whence for $\theta = \pi/2$ we find $L_0 = 1.1 \pm 0.1\ 10^{-2}\ F(T, n_\mathrm{H})$ erg s^{-1} cm^{-2} for the CDDM $(\alpha = 2)$, and $L_0 = 2.0 \pm 0.2\ 10^{-3}\ F(T, n_\mathrm{H})$ erg s^{-1} cm^{-2} for the NCDDM $(\alpha = 0)$.

In Table 2, all of the above results are summarised for both sets of models, and four values of α. Notice that the velocity of the wind and intrinsic luminosities are higher for the CDDM than for the NCCDM, although the mass-loss rates, and densities are higher in the NCDDM. In general, values for these parameters increase as α varies from 0 to 3.

6. Conclusions

We have undertaken multi-slit low and high resolution spectroscopy, together with narrow band imaging of the unusual bilobal outflow source NGC 6905. Our results reveal substantial variations in relative line strengths over the nebula, arising perhaps through stratification and/or shock excitation – with, in particular, substantial enhancement in low excitation [N II] emission towards the northerly and southerly ansae. A major result is the evaluation of the source kinematics, and the construction of two dimensional projected velocity maps for both the principal, interior spheroidal shell, and external lobes. Application of a simple, tilted symmetric model to this data suggest that the observed kinematics may be accounted for excellently, providing the expansion properties of the lobes and spheroid are different.

Taking all the evidence together, we have proposed a model for the source which, we believe, is broadly capable of explaining (i) the observed kinematics of the lobes (albeit these are least well established); (ii) the source morphology, (iii) the variation in

source excitation; and (iv) the location and presence of the ansae. In this model, we suppose that the outer lobes are a consequence of shock interaction between an outflowing wind and external neutral halo. The nature of the inner spheroidal shell is unclear, but may take the form of a photoionized envelope responsible for wind collimation (our preferred option), or be itself the consequence of shock interaction; both options are qualitatively supported through more detailed analysis.

Applying a generalised form the shock analysis by Cantó (1980) and Barral & Cantó (1981) to the present case, and in particular, assuming a spherically symmetric decrement in exterior halo densities, we then show that lobal morphology is not seriously dependent upon the rate of decrement of halo densities, or upon the precise nature of the shock interface interior to the lobes. Similarly, although our detailed models are chosen for pedagogical reasons alone, the ranges of wind velocity are predicted to fall in a relatively narrow range $\sim 0.5 \rightarrow 1.0\ 10^3\ \mathrm{km\,s^{-1}}$ – similar to values observed in other PN. Mass-loss rates $\sim 10^{-7}\ M_\odot\ \mathrm{yr}^{-1}$ are similarly low, and consistent with estimates for other nebulae possessing hot central stars.

Acknowledgements. The authors thank Dr. P. G. Williams for several helpful comments, whilst JPP also thanks DGICYT for extending a Visiting Professorship over this period. The 2.5 m INT is operated on the island of La Palma by the Royal Greenwich Observatory in the Spanish Observatorio del Roque de los Muchachos of the Instituto de Astrofisica de Canarias. This research was partially funded through grant n. PB 89-0510, from the Dirección General de Investigación Científica y Técnica of the spanish Ministerio de Educación y Ciencia.

References

Acker A., Gleizes F., Chopinet M., et al., 1982, Catalogue of the Central Stars of True and Possible Planetary Nebulae, Observatoire de Strasbourg
Allen C. W., 1964, Astrophysical Quantities, Athlone Press, London
Aller L. H., 1956, Gaseous Nebulae, Wiley (ed.), New York
Aller L. H., Epps H. W., ApJ 204, 445
Aller L., 1984, Physics of Thermal Gaseous Nebulae, Reidel, Dordrecht
Balick B., 1987, AJ 94, 671
Barral J. F., Cantó J., 1981, Rev. Mex. Astron. Astrofis. 5, 101
Benvenuti P., Perinotto M., 1980, Proc Second IUE Conf., p. 187
Calvet N., Peimbert M., 1983, Rev. Mex. Astron. Astrofis. 5, 319
Cantó J., 1978, A & A 70, 111
Cantó J., 1980, A & A 86, 327
Cantó J., 1983, Rev. Mex. Astron. Astrofís. 7, 109
Cantó J., Rodriguez L. F., 1983, ApJ 239, 982
Cantó J., Tenorio-Tagle G., Różyczka M., 1988, ApJ 192, 287
Castor J. L., Lutz J.H., Seaton M. J., 1981, MNRAS 194, 547
Cuesta L., Phillips J. P., Mampaso A., 1990, New Windows to the Universe, ERAM Symp. XI, Ap & SS 171, 163
Cuesta L., Phillips J. P., Mampaso A., 1991, Astronomers Look to the Future, ERAM Symp. XII
Cox D.P., ApJ 178, 143
Dalgarno A., McCray R.A., 1972, ARA&A 10, 375
Eichler D., 1982, ApJ 263, 571
Falle S. A. E. G., Innes D. E., Wilson M. J., 1987, MNRAS 225, 741
Feibelman W. A., 1982, ApJ 258, 562
Feibelman W. A., Aller L. H., 1987, ApJ 319, 407
Fleischer A. J., Gauger A., Seldmayr E., 1991, A & A 242, L1
Friend D. B., Abbott D. C., 1986, ApJ 311, 701
Gurzadyan G. A., 1970, Planetary Nebulae, D. G. Hummer (ed.), Reidel, Dordrecht
Hartigan P., Raymond J., Hartman L., 1987, ApJ 316, 323
Hartmann L., Edwards S., Avrett E., 1982, ApJ 261, 279
Hartmann L., MacGregor K. B., 1980, ApJ 242, 260
Johnson H. M., 1976, ApJ 208, 127
Johnson H. M., 1981, ApJ 250, 590
Kahn F. D., 1980, A & A 83, 303
Kahn F. D., West K. A., 1985, MNRAS 212, 837
Kaler J. B., 1986, ApJ 308, 322
Kaler J. B., Shaw R. A., 1984, ApJ 278, 195
Köppen J., Wehrse R., 1980, Proc. Second IUE Conf., p. 191
Louise R., 1982, A&A 114, 205
Louise R., Hua C. T., 1984, Ap & SS 105, 139
Maciel W. J., 1984, A & AS 55, 253
Meaburn J., Walsh J. R., 1980, MNRAS 191, 5p
Meaburn J., Walsh J. R., 1980, MNRAS 193, 631
Osterbrock D. E., 1974, Astrophysics of Gaseous Nebulae, W. H. Freeman (ed.), Co., San Francisco
Perek L., Kohoutek L., 1967, Catalogue of Galactic Planetary Nebulae, Academic Publishing House of the Czechoslovakian Academy of Science, Prague
Perinotto M., 1983, Planetary Nebulae, I.A.U. Symp. 103, D. R. Flower (ed.), Reidel, Dordrecht, p. 323
Phillips J. P., 1984, A & A 137, 92
Phillips J. P., 1989, Planetary Nebulae, I.A.U. Symp. 131, S. Torres-Peimbert (ed.), Reidel, Dordrecht, p. 425
Phillips J. P., 1990, New Windows to the Universe, ERAM Symp. XI, F. Sánchez, M. Vázquez (eds.), Cambridge Univ. Press. Cambridge, p. 299
Phillips J. P., Mampaso A., 1989, Planetary Nebulae, I.A.U. Symp. 131, S. Torres-Peimbert (ed.), Reidel, Dordrecht, p. 194
Phillips J. P., Pottasch S. R., 1984, A & A 130, 91
Phillips J. P., Reay N. K., 1977, A & A 59, 91
Phillips J. P., White G. J., Harten R., 1985, A & A 145, 118
Phillips J. P., Williams P. G., Mampaso A., Ukita N., 1991, Ap&SS 185, 171
Pottasch S. R., 1983, Planetary Nebulae, Reidel, Dordrecht
Rodríguez L. F., Garcia-Barreto J. A., Cantó J., et al., 1985, MNRAS 215, 353
Sabbadin F., Gratton R. G., Bianchini A., Ortolani, 1984, A & A 136, 181
Sabbadin F., Hamzaoglu E., 1982, A & A 110, 105
Sabbadin F., Hamzaoglu E., 1982, A & AS 50, 1
Sanduleak N., 1971, ApJ 164, 171
Silvestro G., Robberto M., 1987, Planetary and Proto-planetary Nebulae, From IRAS to ISO, A. Preite-Martinez (ed.), Reidel, Dordrecht, p. 107
Smith L., Aller L. H., 1969, ApJ 157, 1245
Smith M. D., 1986, MNRAS 223, 57
Stanghellini L., Kaler J. B., 1989, ApJ 343, 811
Stone R. P. S., 1977, ApJ 218, 767
Weedman D. W., 1968, ApJ 153, 49
Weinberger R., 1989, A & AS 78, 301
Whitford A. E., 1958, AJ 63, 201
Wilson O. C., 1950, ApJ 111, 279
Wilson O. C., 1958, Rev. Modern Phys. 30, 1025